IEEE Open Journal of
Power Electronics

Received 20 April 2022; accepted 13 May 2022. Date of publication 20 May 2022;
date of current version 7 June 2022. The review of this article was arranged by Associate Editor Giovanni De Carne.

Digital Object Identifier 10.1109/OJPEL.2022.3176023

A Mode Switching-Based Decentralized Secondary Control for Microgrids With Hybrid Droop and Master-Slave Structure

JIAZHI WANG [1] (Graduate Student Member, IEEE), ZENG LIU [1] (Member, IEEE), JINJUN LIU [1] (Fellow, IEEE), AND TENG WU [1,2] (Member, IEEE)

[1]State Key Lab of Electrical Insulation and Power Equipment, School of Electrical Engineering, Xi'an Jiaotong University, Xi'an 710049, China
[2]KINGSI Power Co., Ltd., Shanghai 201201, China

CORRESPONDING AUTHOR: ZENG LIU (e-mail: zengliu@mail.xjtu.edu.cn)

This work was supported in part by the National Key Research and Development Program of China under Grant 2018YFB1503101 and in part by the Natural Science Basic Research Program of Shaanxi under Grant 2020JM-060.

ABSTRACT The hybrid droop and master-slave structure studied in existing work complements the advantages of droop control and master-slave control, at the cost of frequency and voltage deviations in microgrids. To eliminate these deviations and maintain accurate power sharing among distributed generators, this paper proposes a decentralized secondary control method based on mode switching, where the secondary controller switches among three modes. In the first mode, a feedback strategy is applied to maintain accurate power sharing among slave distributed generators, and then the load demand is estimated and redistributed among distributed generators to calculate new secondary control commands in the second mode, which are further updated in the third mode to eliminate frequency and point-of-common-coupling bus voltage deviations. The proposed method is communication-free and is able to eliminate the influence of triggering delay among slave distributed generators during the mode switching. The effectiveness of the proposed method is verified through hardware experiments.

INDEX TERMS Decentralized secondary control, droop control, master-slave control, microgrid, mode switching.

NOMENCLATURE

m, s, i (i=1, 2, …, N)	Subscripts denote the master, the slave and the ith slave distributed generators (DGs).
R_{cm}, R_{csi}, X_{cm}, X_{csi}	Cable resistance and reactance.
v_{Cdm}, v_{Cqm}, v_{Cdsi}, v_{Cqsi}	d-axis and q-axis capacitor voltage.
i_{odm}, i_{oqm}, i_{odsi}, i_{oqsi}	d-axis and q-axis output current.
v^*_{dm}	d-axis capacitor voltage reference.
ω_0, E_{b0}	Nominal frequency and point-of-common-coupling (PCC) voltage.
ω^*_m, E^*_{bm}	Frequency and PCC voltage references.
ω^{Mea}_{si}, E^{Est}_{bsi}	Measured frequency and estimated PCC voltage.
ω_{si}, E_{bsi}	Frequency and PCC voltage filtered by low-pass-filters (LPFs).
ω^{Sam}_{si}, E^{Sam}_{bsi}	Sampled frequency and PCC voltage.
P_{0m}, Q_{0m}	Nominal power.
p_m, q_m, p_{si}, q_{si}	Measured instantaneous power.
P_m, Q_m, P_{si}, Q_{si}	Instantaneous power filtered by LPFs.
P^*_{si}, Q^*_{si}	Output power references.
P^{*Sam}_{si}, Q^{*Sam}_{si}	Sampled output power references.
P^{Est}_m, Q^{Est}_m	Estimated output power.
P^{Est}_s, Q^{Est}_s	Estimated output power of all slave DGs.
P_L, Q_L	Estimated load demand.
P_{Lsi}, Q_{Lsi}	Load demand shared by slave DG i.
P_{rsi}, Q_{rsi}	Active and reactive power ratings.
m_{pm}, n_{qm}, m_{psi}, n_{qsi}	Droop gains.
ω_{cm}, ω_{cs}, ω_f	Cutoff frequency of LPFs.

ω_L, ω_H, E_{bL}, E_{bH}	Frequency and PCC voltage boundaries of the pre-configured error band.
α_p, α_q, β_p, β_q	Parameters of the proposed secondary control methods.
γ_{psi}, γ_{qsi}	Power dispatch coefficients.
P_{nsi}, Q_{nsi}	Secondary control commands, also the power setpoints and droop offsets.
P_{nsi}^{New}, Q_{nsi}^{New}	New secondary control commands.
T_{d1}, T_{d2}, T_{d3}	Pre-configured time intervals.
t_d, $t_{d,max}$	Triggering delay and the maximum possible triggering delay.

I. INTRODUCTION

Existing methods for power distribution among distributed generators (DGs) in microgrids can be classified into two categories: the peer-to-peer control, represented by the droop control, and the master-slave control [1]. On the one hand, the awesome active power-frequency (P-ω) and reactive power-voltage (Q-E) droop control is capable of accurate power sharing among voltage-controlled parallel DGs with a communication-free manner, especially for DGs with the same type [2], [3]. On the other hand, the master-slave control is a very simple structure to integrate voltage-controlled and current-controlled parallel DGs in microgrids with several limitations: the single-point-failure problem, poor power quality in remote buses and large capacity requirement for the master DG [4], [5]. Therefore, to complement the advantages of droop control and master-slave control, the hybrid droop and master-slave (HDMS) structure has been studied by many researchers [6]–[8]. In this method, all voltage-controlled DGs are grouped together as master DGs adopting traditional P-ω and Q-E droop control, whereas the rest of current-controlled DGs are grouped together as slave DGs adopting frequency-active power (ω-P) and voltage-reactive power (E-Q) droop method. Using this method, voltage-controlled and current-controlled DGs work together in one microgrid with a simple structure and the load demand would be shared among master DGs and slave DGs with a completely communication-free manner. Meanwhile, the single-point-failure problem along with power quality and capacity issues would be mitigated by proper placement of multiple voltage-controlled DGs in microgrids. However, the secondary control is still required to eliminate frequency and voltage deviations resulting from droop characteristics of master DGs. On this issue, either master DGs or slave DGs can participate in secondary control. Considering most of DGs, such as photovoltaic and wind turbine, operate in the maximum power point tracking mode to generate power as much as possible, current-controlled DGs are dominant in microgrids [9]. Therefore, it is more reasonable to implement secondary control in slave DGs to mitigate the capacity requirement for master DGs.

Generally, secondary control methods can be classified into three groups: centralized, distributed and decentralized schemes [10]. In the centralized scheme, a microgrid central controller (MGCC) communicates with each DG to regulate frequency and voltage, at the expense of low reliability and high cost [11]. As an improvement, requiring only sparse communications, the distributed scheme based on consensus algorithm attracts tremendous interests over the years [12]–[14]. However, communication still challenges the reliability and convergence speed of this technology.

Without communication and MGCC, the decentralized scheme is an optimal solution to achieve the two main control objectives of secondary control: 1) eliminating frequency and voltage deviations and 2) maintaining accurate power sharing. However, the most popular proportional (P) and proportional-integral (PI) regulators can only achieve either of the objectives. P regulators show steady-state frequency and voltage deviations and PI regulators accumulate integral errors that deteriorate power sharing performances [15], [16]. To realize all two objectives, there are two strategies: the single mode strategy where the two objectives are realized in a single mode simultaneously, and the mode switching strategy where the controller switches among several modes in a time division manner and each mode realizes one or part of one objective independently. Many researchers focus on the single mode strategy. The washout filter studied in [17]–[19] is a simple structure to achieve the two secondary control objectives with bandwidth-dependent accuracy. Meanwhile, estimating other DGs' information through nonlinear observers, the state estimation-based methods have been studied in many papers [20]–[22]. Unfortunately, high order matrix calculation and model dependency limit its applications. Furthermore, the injected small-AC-signal in [23] acts as the communication link but weakens the voltage quality and complicates the overall control structure. Fortunately, the mode switching strategy achieves each objective with independent modes resulting in higher accuracy, lighter calculation burden and easier realization. Secondary control in [24] switches between P and PI regulators to eliminate frequency and voltage deviations and maintain accurate power sharing simultaneously. However, the required event trigger process makes the system fragile suffering possible triggering delay among DGs.

To tackle the possible triggering delay in aforementioned mode switching-based secondary control methods, this paper extends our previous work in [25] and proposes a new mode switching-based decentralized secondary control method for microgrids with HDMS structure, which is only implemented in the slave DGs so that the capacity of the master DG can be greatly reduced. In this method, the secondary controllers switch among three modes to achieve correspond secondary control objectives in a time division manner. In the first mode, i.e., power-sharing mode, a feedback strategy maintains accurate active and reactive power sharing among slave DGs in steady state, then in the second mode, i.e., power-estimation mode, the secondary controllers estimate the load demand and redistribute it among DGs to calculate new secondary control commands (SCCs), which are further updated in the third mode, i.e., restoration mode, so that frequency and PCC voltage would restore to their nominal values. The main

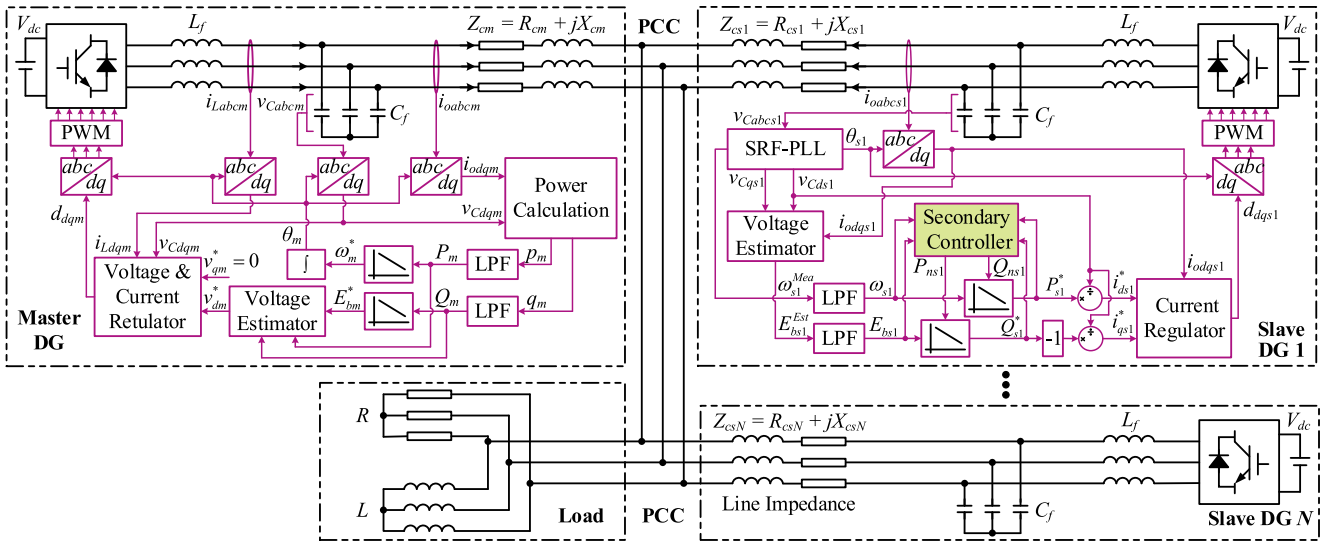

FIGURE 1. Studied microgrid with hybrid droop and master-slave structure.

contributions of this paper are summarized as follows. First, frequency and PCC voltage would recover without deteriorating power sharing performances. Meanwhile, to resist the perturbations in microgrids, an error band is introduced to instruct the triggering and termination operations of secondary control. Second, the influence of any possible triggering delay among slave DGs can be eliminated theoretically. Finally, a simplified model is established for analysis and parameters design.

The rest of this paper is organized as follows. Section II describes system overall structures. Section III introduces the proposed secondary control method. Some applications issues involving modeling, analysis and parameters design are discussed in Section IV. The experimental results are presented in Section V. Finally, the concluding remarks are given in Section VI.

II. SYSTEM STRUCTURE

Fig. 1 shows the structure of the studied islanded microgrid with N+1 DGs and RL loads connected to the same PCC bus. Each DG consists of an ideal DC power supply, a three-phase inverter, an LC output filter and transmission cables. The HDMS structure is applied to the studied microgrid with only one master DG considered to simplify the analysis. However, the proposed method can be naturally applied to the HDMS structure with a group of master DGs.

A. MASTER DG

The voltage-controlled DG is considered as the master DG in the studied system. The master DG first uses capacitor voltages and output currents to calculate the instantaneous power

$$p_m = v_{Cdm} i_{odm} + v_{Cqm} i_{oqm}, \tag{1a}$$

$$q_m = v_{Cqm} i_{odm} - v_{Cdm} i_{oqm}. \tag{1b}$$

Then, the average values of active and reactive powers are obtained through LPFs with transfer function shown as follows:

$$G_{LPFm}(s) = \omega_{cm}/(s + \omega_{cm}). \tag{2}$$

After that, the traditional droop control is applied to calculate the frequency and the PCC voltage references:

$$\omega_m^* = \omega_0 - m_{pm}(P_m - P_{0m}), \tag{3a}$$

$$E_{bm}^* = E_{b0} - n_{qm}(Q_m - Q_{0m}). \tag{3b}$$

Since the DG can only have access to capacitor voltage, the d-axis capacitor voltage reference can be estimated using PCC voltage reference E_{bm}^* and cable impedance information prestored in the local controller based on the phasor analysis:

$$v_{dm}^* = \sqrt{0.5E_{bm}^{*2} + P_m R_{cm} + Q_m X_{cm} + 0.5\sqrt{\Delta}}, \tag{4a}$$

$$\Delta = E_{bm}^{*4} + 2(P_m R_{cm} + Q_m X_{cm}) E_{bm}^{*2} - 4(P_m X_{cm} - Q_m R_{cm})^2. \tag{4b}$$

Meanwhile, the q-axis reference is set to zero. Finally, the inner loops adopt traditional PI-based dual loops control in dq-frame.

B. SLAVE DG

All current-controlled DGs are grouped together as the slave DGs. Each slave DG first measures the frequency and the capacitor voltage through a synchronous-reference-frame phase-locked-loop (SRF-PLL). And then, the PCC bus voltage can be estimated using the measurements and the cable impedance information prestored in the local controller of each slave DG so that estimation is completely communication-free. To do this, the instantaneous powers are calculated

$$p_{si} = v_{Cdsi} i_{odsi} + v_{Cqsi} i_{oqsi}, \tag{5a}$$

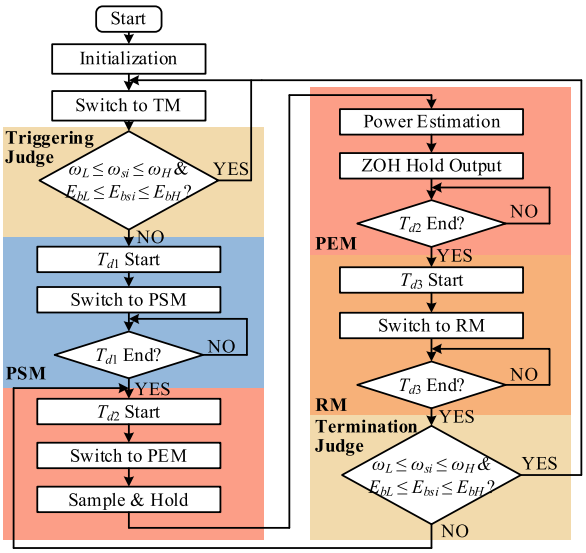

FIGURE 2. Timer-based mode switching rules of the proposed method.

$$q_{si} = v_{Cqsi} i_{odsi} - v_{Cdsi} i_{oqsi}. \tag{5b}$$

Then, similar to the master DG, the average values of the active and the reactive power P_{si} and Q_{si} are obtained through LPFs with transfer function shown as follows:

$$G_{LPFs}(s) = \omega_{cs}/(s + \omega_{cs}). \tag{6}$$

Since the q-axis capacitor voltage tracks zero through SRF-PLL. According to phasor analysis, the PCC voltage can be estimated as

$$E_{bsi}^{Est} = \sqrt{\left(v_{Cdsi} - \frac{P_{si}R_{csi} + Q_{si}X_{csi}}{v_{Cdsi}}\right)^2 + \left(\frac{P_{si}X_{csi} - Q_{si}R_{csi}}{v_{Cdsi}}\right)^2}. \tag{7}$$

To resist the perturbations in microgrids, the measured frequency and the estimated voltage are filtered through LPFs with the same transfer function as (6) . Then, the ω-P and E-Q droop control are applied to calculate the power references as (8a) and (8b) shows, where P_{nsi} and Q_{nsi} are power setpoints, or named SCCs, to be calculated by the secondary controller. Finally, after calculating the d-axis and q-axis current references, the traditional PI-based current regulators are adopted in the inner loop.

$$P_{si}^* = -m_{psi}(\omega_{si} - \omega_0) + P_{nsi}, \tag{8a}$$

$$Q_{si}^* = -n_{qsi}(E_{bsi} - E_{b0}) + Q_{nsi}. \tag{8b}$$

III. PROPOSED MODE SWITCHING-BASED DECENTRALIZED SECONDARY CONTROL METHOD

In the proposed mode switching-based secondary control method, only the slave DGs participate in secondary frequency and PCC voltage regulation so that the required capacity of the master DG to deal with the load variations can be greatly reduced, considering the current-controlled slave DGs certain dominate in the microgrids as Fig. 1 shows.

Fig. 2 shows the timer-based mode switching rules. An error band instructs the triggering and termination of the secondary control. When secondary control terminates, the secondary controllers operate in the termination mode (TM) and maintain their outputs. However, when secondary control is triggered, the controllers switch among three modes: the power-sharing mode (PSM), the power-estimation mode (PEM) and the restoration mode (RM). Each of these three modes achieves one control goal and will last for a preset time interval T_{d1}, T_{d2} and T_{d3} respectively, controlled by a timer. In PSM, any power sharing error among slave DGs resulting from measurement noise and the possible estimation errors would be eliminated. Then, in PEM, the secondary controllers calculate new SSCs, which are also the power setpoints of slave DGs, based on load demands estimation and redistribution. Finally, in RM, the new SSCs are updated to recover frequency and PCC voltage. Details for each mode are illustrated in Fig. 3.

A. TERMINATION MODE (TM)

After initialization, the secondary controller switches to TM. In this mode, the secondary controller maintains its outputs and monitors whether frequency and PCC voltage meet the triggering condition.

B. TRIGGERING CONDITION

To resist small perturbations in microgrids, an error band is introduced. When both of the frequency and the PCC voltage stay in the error band, the secondary control would stay in TM, otherwise the secondary control would be triggered. The error band is expressed as

$$\omega_L \le \omega_{si} \le \omega_H \text{ and } E_{bL} \le E_{bsi} \le E_{bH}. \tag{9}$$

C. POWER-SHARING MODE (PSM)

When frequency or PCC voltage exceeds the error band, secondary control is triggered and switched to PSM immediately. The PSM will last for a given time interval T_{d1}, controlled by the timer. The control goal in this mode is to guarantee accurate active and reactive power sharing among slave DGs. To achieve this, feedback loops and feedforward loops are added together to form SCCs. The feedback loops are responsible for eliminating power sharing errors and the feedforward loops provide another degree-of-freedom for steady state and dynamic performances improvement. The LPFs with a cut-off frequency of ω_f determine the bandwidth of secondary controllers. This control law can be expressed as

$$P_{nsi} = \frac{\omega_f}{s + \omega_f}\left[\frac{\omega_{cs}}{s + \omega_{cs}}\alpha_p P_{si}^* + \frac{\beta_p \gamma_{psi}}{m_{pm}}(\omega_0 - \omega_{si})\right], \tag{10a}$$

$$Q_{nsi} = \frac{\omega_f}{s + \omega_f}\left[\frac{\omega_{cs}}{s + \omega_{cs}}\alpha_q Q_{si}^* + \frac{\beta_q \gamma_{qsi}}{n_{qm}}(E_{b0} - E_{bsi})\right]. \tag{10b}$$

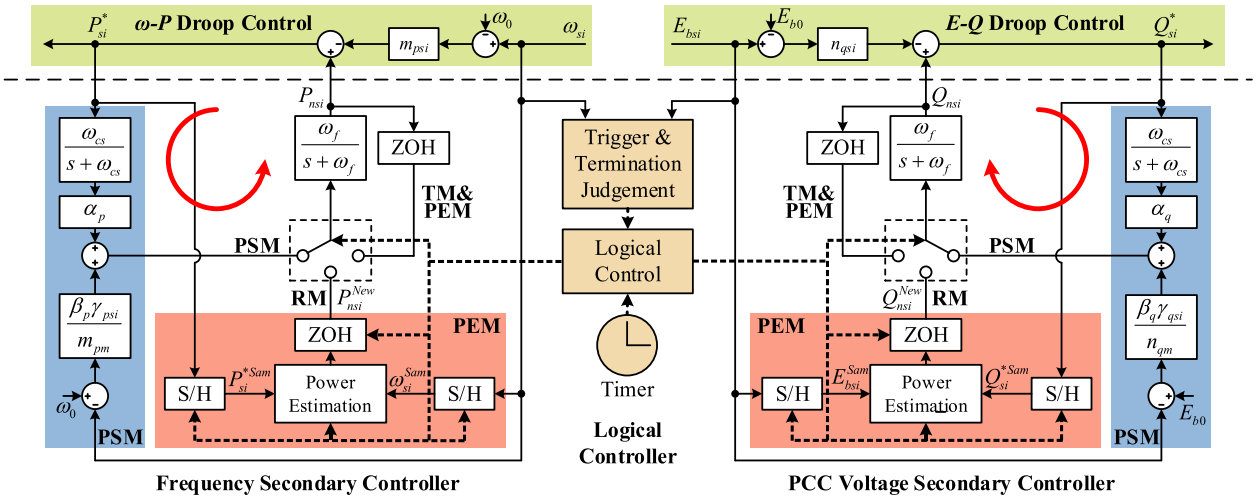

FIGURE 3. Overall control structure of proposed secondary control method composed of frequency secondary controller, PCC voltage secondary controller, and logical controller. ("S/H" means sample and hold, "ZOH" means zero-order-holder).

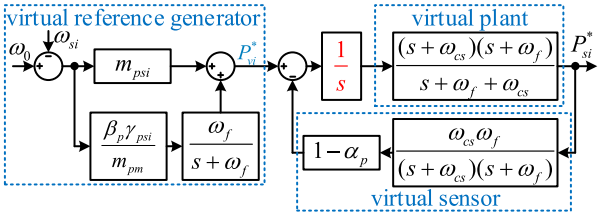

FIGURE 4. Rearranged block diagram of frequency secondary controller in PSM.

Where $\alpha_p<1$, $\alpha_q<1$, $\beta_p>0$, $\beta_q>0$, γ_{psi} and γ_{qsi} are power dispatch coefficients that are proportional to the droop gains

$$\gamma_{psi} = m_{psi} \Big/ \sum\nolimits_{i=1}^{N} m_{psi}, \tag{11a}$$

$$\gamma_{qsi} = n_{qsi} \Big/ \sum\nolimits_{i=1}^{N} n_{qsi}. \tag{11b}$$

After rearranging the block diagram of the frequency secondary controller in PSM, as Fig. 4 shows, an integrator appears in the feedforward path that can be treated as virtual regulator. Since the frequency deviations in steady state sensed by each slave DG is the same, and γ_{psi} is proportional to the droop gain m_{psi}, the virtual reference P_{vi}^* would also be proportional to the droop gains. As a result, the power reference P_{si}^* is forced to track the proportionate virtual reference P_{vi}^* through an integral regulator. It is apparent that the power reference will be shared among slave DGs in steady state. Therefore, the output power will be shared among slave DGs in steady state in the same proportion, if the inner control loops are well designed. The same conclusion can be drawn when combining (10a), (10b) with (8a), (8b). In steady state, the relationships between frequency and PCC voltage deviations and power references are

$$P_{si}^* = \frac{\gamma_{psi}}{1-\alpha_p}\left(\sum_{i=1}^{N} m_{psi} + \frac{\beta_p}{m_{pm}}\right)(\omega_0 - \omega_{si}), \tag{12a}$$

$$Q_{si}^* = \frac{\gamma_{qsi}}{1-\alpha_q}\left(\sum_{i=1}^{N} n_{qsi} + \frac{\beta_q}{n_{qm}}\right)(E_{b0} - E_{bsi}). \tag{12b}$$

Since the slave DGs share the same frequency and PCC voltage deviations in steady state, the power references would be shared according to the power dispatch coefficients γ_{psi} and γ_{qsi} in steady state. Finally, the output power of slave DGs would also be shared in the same proportion in steady state, as (13a) and (13b) shows, if the inner control loops are well designed.

$$P_{s1}^* : P_{s2}^* : \cdots : P_{sN}^* = P_{s1} : P_{s2} : \cdots : P_{sN} = \gamma_{ps1} : \gamma_{ps2} : \cdots : \gamma_{psN}, \tag{13a}$$

$$Q_{s1}^* : Q_{s2}^* : \cdots : Q_{sN}^* = Q_{s1} : Q_{s2} : \cdots : Q_{sN} = \gamma_{qs1} : \gamma_{qs2} : \cdots : \gamma_{qsN}. \tag{13b}$$

D. POWER-ESTIMATION MODE (PEM)

If T_{d1} is long enough so that system achieves steady state at the end of PSM, then the output power of slave DGs shares according to (13a) and (13b). After T_{d1} timing out, secondary control switches to PEM immediately and lasts for time interval T_{d2}. During this mode, the secondary controller maintains its output, just like in TM. The control goal is to calculate the new SCCs based on load demand estimation. To do this, the frequency, PCC voltage and power in steady state are sampled and hold firstly. Then, as Fig. 5 illustrated, the load demand can be estimated based on two facts:

1) The frequency and PCC voltage in steady state sensed by each DG are the same, which means $\omega_m^* = \omega_{si}^{Sam}$ and $E_{bm}^* = E_{bsi}^{Sam}$, so that the power of the master DG can

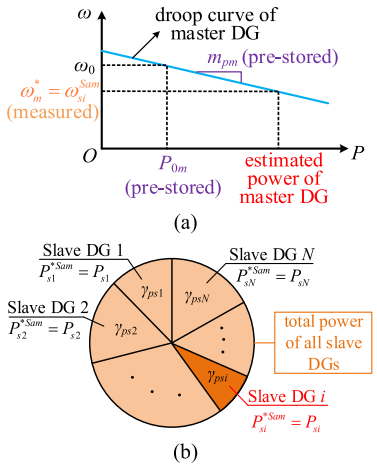

FIGURE 5. Principle of load active power estimation. (a) Power estimation of the master DG. (b) Estimation of total power of all slave DGs.

be estimated according to its droop control law (3a) and (3b) as

$$P_m^{Est} = P_{0m} + \left(\omega_0 - \omega_{si}^{Sam}\right)/m_{pm}, \tag{14a}$$

$$Q_m^{Est} = Q_{0m} + \left(E_{b0} - E_{bsi}^{Sam}\right)/n_{qm}. \tag{14b}$$

Where P_{0m}, Q_{0m}, $\mathrm{m_{pm}}$ and n_{qm} can be prestored in the local controller of each slave DG so that the estimation is completely communication-free.

1) The PSM guarantees the power sharing in steady state as (13a) and (13b) describes so that total output power of all slave DGs can be estimated by each slave DG by its power dispatch coefficients and its power sampling, which equals to its output power if inner loops are well designed as

$$P_s^{Est} = P_{si}^{*Sam}/\gamma_{psi}, \tag{15a}$$

$$Q_s^{Est} = Q_{si}^{*Sam}/\gamma_{qsi}. \tag{15b}$$

Finally, neglecting the transmission loss, the load demand can be estimated by adding up the estimation of master DG's power and total power of all salve DGs together as

$$P_L = P_m^{Est} + P_s^{Est} = P_{si}^{*Sam}/\gamma_{psi} + P_{0m} + \left(\omega_0 - \omega_{si}^{Sam}\right)/m_{pm}, \tag{16a}$$

$$Q_L = Q_m^{Est} + Q_s^{Est} = Q_{si}^{*Sam}/\gamma_{qsi} + Q_{0m} + \left(E_{b0} - E_{bsi}^{Sam}\right)/n_{qm}. \tag{16b}$$

After that, the estimated load demand should be redistributed among the N+1 DGs. To restore frequency and PCC voltage to their nominal values, the master DG should undertake their nominal power P_{0m} and Q_{0m} according to (3a) and (3b). Meanwhile, the rest of load demand should be shared among slave DGs based on their power dispatch coefficients γ_{psi} and γ_{qsi}. Therefore, the load demand undertaken by the ith slave DG can be derived from (16a) and (16b)

$$P_{Lsi} = \gamma_{psi}(P_L - P_{0m}) = P_{si}^{*Sam} + \gamma_{psi}\left(\omega_0 - \omega_{si}^{Sam}\right)/m_{pm}, \tag{17a}$$

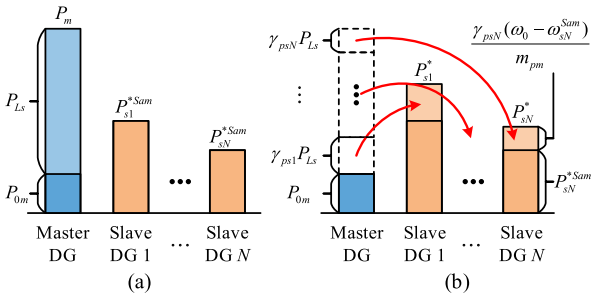

FIGURE 6. Physical Meaning of (18a). (a) Before power redistributing. (b) After power redistributing.

$$Q_{Lsi} = \gamma_{qsi}(Q_L - Q_{0m}) = Q_{si}^{*Sam} + \gamma_{qsi}\left(E_{b0} - E_{bsi}^{Sam}\right)/n_{qm}. \tag{17b}$$

Finally, to eliminate frequency and PCC voltage deviations, let ω_{si}=ω_0 and $P_{si}^* = P_{Lsi}$ for (8a), E_{bsi}=E_{b0} and $Q_{si}^* = Q_{Lsi}$ for (8b), the new SCCs can be calculated as

$$P_{nsi}^{New} = P_{Lsi} = P_{si}^{*Sam} + \gamma_{psi}\left(\omega_0 - \omega_{si}^{Sam}\right)/m_{pm}, \tag{18a}$$

$$Q_{nsi}^{New} = Q_{Lsi} = Q_{si}^{*Sam} + \gamma_{qsi}\left(E_{b0} - E_{bsi}^{Sam}\right)/n_{qm}. \tag{18b}$$

The calculated new SCCs will then be hold by zero-order-holders and be updated until T_{d2} timing out. They cannot be updated immediately, otherwise the system will move from steady state to transient state and the possible triggering delay among slave DGs, which will be discussed in the following part, will make the frequency, PCC voltage and power references sampling of the delay-triggered slave DGs differ from the sampling of non-delayed slave DGs. As a result, power estimation error will appear.

Fig. 6 illustrates the physical meaning of (18a). After power redistributing, the master DG only undertakes P_{0m} and the rest of load demand is shared by the N slave DGs according to their γ_{psi}. Each slave DG undertakes its current sampled power P_{si}^{*Sam} and the shared power $\gamma_{psi}\left(\omega_0 - \omega_{si}^{Sam}\right)/m_{pm}$.

E. RESTORATION MODE (RM)

After T_{d2} timing out, the secondary control switches to RM immediately and lasts for a time interval T_{d3}. The control goal in this mode is to restore frequency and PCC voltage. To achieve this, the outputs of secondary controllers would be updated by the new calculated SCCs stored in ZOHs through LPFs, whose cutoff frequency determines the restoration speed.

F. TERMINATION JUDGEMENT

During the process from PEM to RM, if load demand shows no variations, frequency and PCC voltage will exactly restore to their nominal values theoretically. Otherwise, frequency and PCC voltage deviations will still appear and even exceed the error band defined in (9) suffering a large load variation. To deal with this issue, a judgement is configured. The termination condition is that only if both the frequency and the

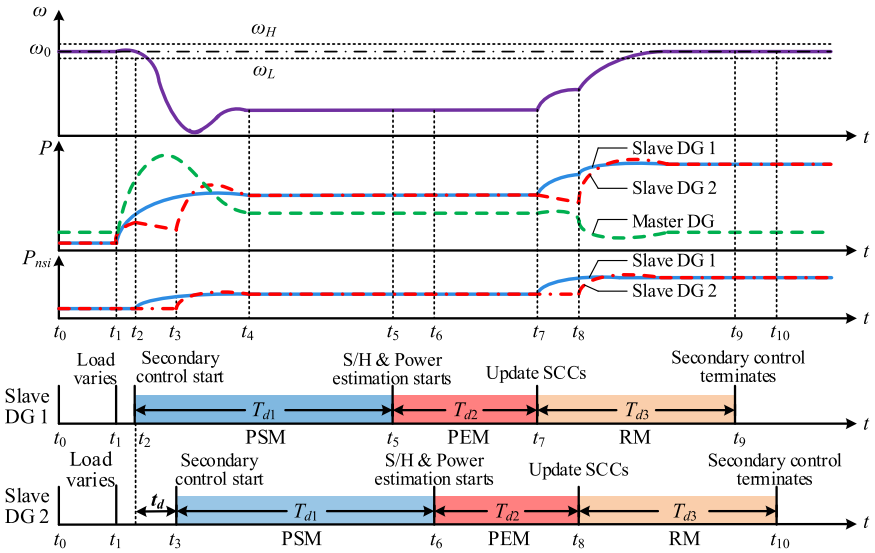

FIGURE 7. The sketch illustrating the example of triggering delay during frequency restoration using the proposed secondary control method. The system consists of one master DG and two slave DGs. The system operates at nominal frequency initially and shows an inertial response with frequency drop when the load demand changes in t_1. When the frequency waveform overlaps the lower boundary of the error band, the secondary control of slave DG 1 is triggered at t_2 and switches to PSM, whereas the secondary control of slave DG 2 is triggered at t_3 with a triggering delay t_d resulting from the hardware or software distinctions. After PSM, the output power of the two slave DGs reaches an agreement owing to the feedback strategy in PSM. Then the new SCCs of the two slave DGs are calculated in PEM and updated in RM in turn so that the frequency recovers to the error band finally.

PCC voltage stay in the error band defined in (9) after RM, the secondary control terminates, otherwise the secondary control would be retriggered and switched to PEM again.

G. EXAMPLES OF TRIGGERING DELAY AND RETRIGGERING

Fig. 7 sketches an example of possible triggering delay, resulting from the software or hardware distinctions among DGs, during the frequency restoration. As the waveforms shown, using the timer-based mode switching strategy, the triggering delay will not change, which means $t_d = t_{10} - t_9 = t_8 - t_7 = t_6 - t_5 = t_3 - t_2$, so that the triggering delay is limited, and its influence can be eliminated. Meanwhile, another example showing the retriggering process during PCC voltage restoration is illustrated in Fig. 8.

IV. APPLICATION ISSUES

This section discusses some issues related to real applications such as modeling, analysis, and parameters design. Considering the similarity between secondary frequency and PCC voltage regulation, only frequency regulation processes are modeled and analyzed as an example.

A. MODELING AND ANALYSIS

As Fig. 9 shows, a simplified model of frequency regulation process only considering droop controllers and secondary controllers is established for qualitive analysis and parameters design purposes. The dynamics related to circuit, inner control loops and SRF-PLLs are much faster so that their dynamics can be neglected.

1) PSM

In PSM, feedback loops and feedforward loops are added up to form the SCCs. The feedback loops contain connotative integrators in feedforward paths so that accurate power sharing can be guaranteed in steady state. According to Fig. 9, the transfer function from load demand variation $\Delta P_L(s) = P_L(s) - P_{0m}$ to frequency deviation $\Delta\omega(s)$ can be derived as

$$\Delta\omega(s) = \frac{m_{pm}\omega_{cm}\left[s^2+(\omega_f+\omega_{cs})s+\omega_f\omega_{cs}(1-\alpha_p)\right]}{s^3+a_2s^2+a_1s+a_0}\Delta P_L(s), \tag{19a}$$

$$a_2 = \omega_{cm} + \omega_{cs} + \omega_f, \tag{19b}$$

$$a_1 = \omega_{cm}\omega_f + \omega_{cs}\omega_f(1-\alpha_p) + \omega_{cm}\omega_{cs} \times \left(1 + m_{pm}\sum_{i=1}^{N} m_{psi}\right), \tag{19c}$$

$$a_0 = \omega_{cm}\omega_{cs}\omega_f\left(1 - \alpha_p + \beta_p + m_{pm}\sum_{i=1}^{N} m_{psi}\right). \tag{19d}$$

The root loci are showing in Fig. 10. With the increase of α_p, the damping ratio of the two conjunction poles increases. But the damping ratio and the phase margin decreases with the increase of β_p.

2) PEM, RM AND TM

In PEM, the secondary controllers maintain their outputs and new SCCs are calculated and then stored in ZOHs. Once switching to RM, the SCCs will be updated by the new calculated ones through LPFs so that frequency and PCC voltage deviations will be eliminated gradually. After the secondary

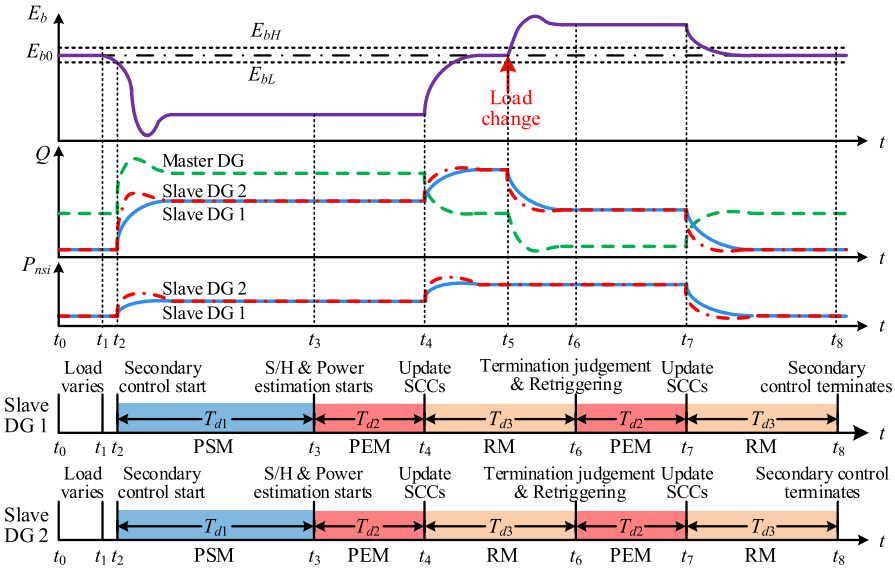

FIGURE 8. The sketch illustrating the example of retriggering process during PCC voltage restoration using the proposed secondary control method. The system consists of one master DG and two slave DGs. The system operates at nominal PCC voltage initially and shows an inertial response with PCC voltage drop when the load demand changes in t_1. When the PCC voltage waveform overlaps the lower boundary of the error band, the secondary control of slave DG 1 and slave DG2 is triggered at t_2 simultaneously. Then after going through PSM, PEM and updating SCCs at t_4, the PCC voltage deviations resulting from load change at t_1 are gradually eliminated. However, the load demand changes again at t_5 and the PCC voltage still stays out of the error band during termination judgement process at t_6 so that the secondary control is retriggered and goes through PEM and RM again to restore PCC voltage. Finally, the PCC voltage restores to its nominal value.

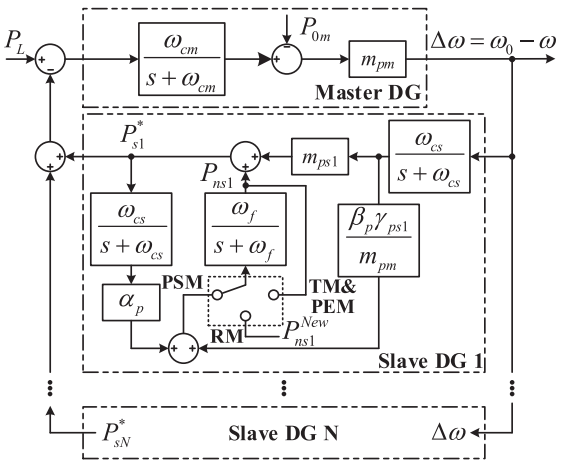

FIGURE 9. The simplified model of frequency regulation process neglecting the dynamics of circuits, inner control loops and SRF-PLLs.

control terminated, the secondary controllers operate in TM and also maintain their outputs. As a result, the SCCs during PEM and TM keep constant and show a step change once switching to RM. According to Fig. 9, the system transfer function can be expressed as

$$\Delta\omega(s) = \frac{m_{pm}\omega_{cm}(s+\omega_{cs})}{s^2+b_1 s+b_0}\left[\Delta P_L(s) - \frac{\omega_f}{s+\omega_f}\sum_{i=1}^{N} P_{nsi}(s)\right], \tag{20a}$$

$$b_1 = \omega_{cm} + \omega_{cs}, \tag{20b}$$

$$b_0 = \omega_{cm}\omega_{cs}\left(1 + m_{pm}\sum_{i=1}^{N} m_{psi}\right). \tag{20c}$$

According to the Routh Criterion, (20a) is always stable since $b_1 > 0$ and $b_0 > 0$. Fig. 11 shows the root locus of the transfer function from $P_{nsi}(s)$ to $\Delta\omega(s)$. The damping ratio decreases with the increase of $\sum_{i=1}^{N} m_{psi}$.

B. PARAMETERS DESIGN

Step 1: Determining ω_L, ω_H, E_{bL} and E_{bH}. According to IEEE standard 1547-2018, frequency and PCC voltage deviations should be limited within ±0.1Hz and ±3% of nominal values in medium voltage network [26]. Therefore, the error band defined in (9) should be designed within this range.

Step 2: Determine γ_{psi} and γ_{qsi}. Generally, the slave DGs shares the load demand according to their rated power, which are determined as

$$\gamma_{psi} = P_{rsi} \Big/ \sum_{i=1}^{N} P_{rsi}, \tag{21a}$$

$$\gamma_{qsi} = Q_{rsi} \Big/ \sum_{i=1}^{N} Q_{rsi}. \tag{21b}$$

Step 3: Determine m_{psi} and n_{qsi}. Setting system damping ratio equal to 0.707, according to (11a), (11b) and (20a), (20b), (20c), m_{psi} and n_{qsi} can be determined as

$$m_{psi} = \gamma_{psi}\sum_{i=1}^{N} m_{psi} = \gamma_{psi}\frac{\omega_{cm}^2 + \omega_{cs}^2}{2m_{pm}\omega_{cm}\omega_{cs}}, \tag{22a}$$

$$n_{qsi} = \gamma_{qsi}\sum_{i=1}^{N} n_{qsi} = \gamma_{qsi}\frac{\omega_{cm}^2 + \omega_{cs}^2}{2n_{qm}\omega_{cm}\omega_{cs}}. \tag{22b}$$

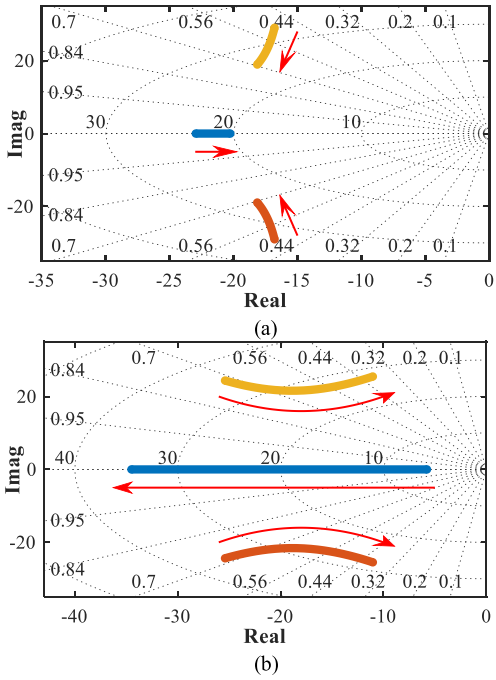

FIGURE 10. Root loci of frequency regulation model in PSM. m_{pm} = 2×10^{-4} [rad/s/W], $\omega_{cm} = \omega_{cs} = 8\pi$ [rad/s], $\sum_{i=1}^{N} m_{psi}$ =5000 [W/(rad/s)], ω_f=2π [rad/s]. (a) α_p increases from -2 to 0.99, β_p =2.5 (b) β_p increases from 0.1 to 5, α_p=0.3.

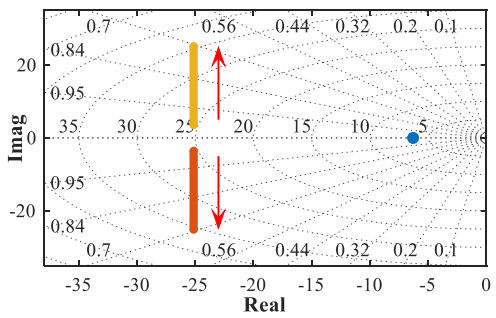

FIGURE 11. Root locus of the transfer function from $P_{nsi}(s)$ to $\Delta\omega(s)$ when the summation $\sum_{i=1}^{N} m_{psi}$ increases from 2 to 5e3 [W/(rad/s)]. m_{pm} = 2×10^{-4} [rad/s/W], $\omega_{cm} = \omega_{cs} = 8\pi$ [rad/s], ω_f=2π [rad/s].

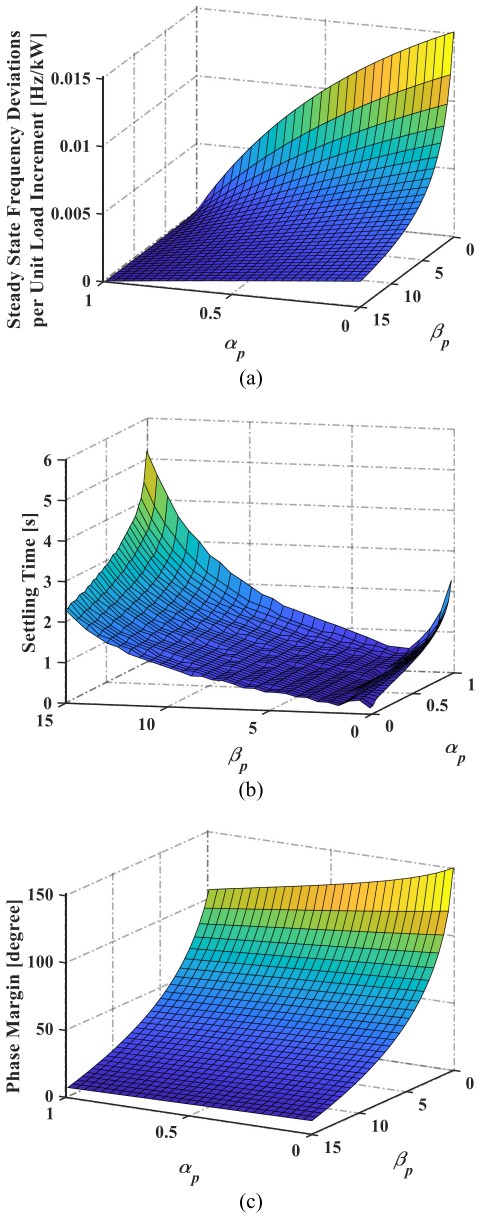

FIGURE 12. Influence of secondary control parameters α_p and β_p on (a) steady state frequency deviations during PSM, (b) settling time (2% error band) and (c) phase margin.

Step 4: Determine ω_f. The ω_f is usually designed smaller than the cutoff frequency of LPFs of droop control for decoupling between the secondary control and the droop control but should not be too small for fast responses.

Step 5: Optimize α_p, α_q, β_p, β_q. These parameters determine the static and dynamic performances of the system in PSM. Therefore, they could be chosen optimally considering some indicators such as the steady state deviations during PSM, settling time and stability margin. Fig. 12 shows the influence of α_p and β_p. α_p=0.3 and β_p=2.5 are selected in this paper with 74.28 degrees phase margin, 0.28 seconds settling time and 0.0053Hz unit steady state frequency deviations during PSM.

Step 6: Determine T_{d1}, T_{d2} and T_{d3}. In PSM, the T_{d1} should be long enough for system reaching the steady state so that slave DGs can accurately share the load demand. Considering that the dynamics of secondary control are much slower than the droop control and mainly determined by LPFs in secondary controllers, T_{d1} should at least be greater than the time constant of LPFs. Meanwhile, secondary controllers shall deal with the possible triggering delay among slave DGs as mentioned in Section IV. Therefore, T_{d1} can be designed as

$$T_{d1} \geq 2\pi/\omega_f + t_{d,max}. \tag{23a}$$

The second time interval T_{d2} deals with the possible triggering delay among slave DGs. Similarly, the T_{d3} guarantees the system reaches steady state before termination judgement.

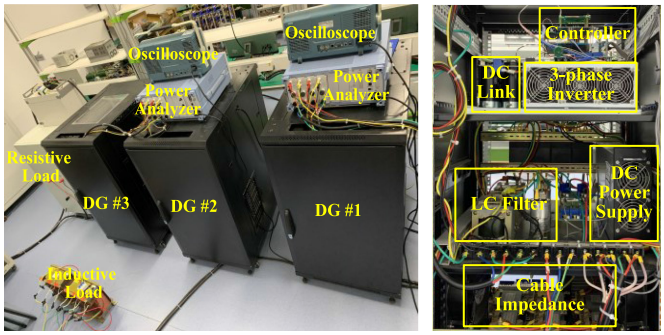

(a) (b)

FIGURE 13. Hardware platform photos of (a) overall system and (b) inside of each DG.

Therefore, they can be roughly designed as

$$T_{d2} = T_{d3} = T_{d1}. \tag{23b}$$

C. COMMUNICATION-FREE CAPABILITY

The operation of the proposed method can be divided into two modes: the configuration mode and the normal operation mode. In the configuration mode, all the required information, such as cable impedance and droop gains of the master DG, wound be prestored in the local controllers of all slave DGs. Then, in the normal operation mode, the proposed method only requires the prestored information along with the local measurements to achieve secondary control targets. Therefore, the operations in the normal operation mode are completely communication-free. However, the system should switch to configuration mode to update some required information once there are some significant changes in the microgrids such as any DG tripped off or any new DG entering service.

V. EXPERIMENTAL VERIFICATION

The effect of the proposed secondary control method is verified through a hardware platform containing three DGs and the loads as Fig. 13 shows. Thereinto, DG #1 is the master DG, and the other two are the slave DGs. Each DG consists of a 10kVA three-phase inverter, an *LC* filter and the cable impedance. The detailed circuit topology follows Fig. 1 and the parameters of circuit and controllers are listed in Table 1. All the aforementioned technologies are implemented in digital-signal-processor (DSP) TMS320F28335 of Texas Instruments. Variables to be observed are calculated in DSP and captured by two Tektronix oscilloscopes (MDO3014 and DPO4014B) through digital-to-analog converters.

First, the tradition PI-based method and the proposed method are compared to verify the effectiveness of the proposed method through case 1 and case 2. Meanwhile, case 2 also verifies the ability of the proposed method to deal with triggering delay of secondary control among slave DGs. Case 3 shows how the proposed method deals with step change in load demand during the secondary control process. The retriggering mechanism works in this situation. Then, the model in Section IV is verified in Case 4. Finally, case 5 shows the voltage and current waveforms of the proposed method.

TABLE 1. Experimental Parameters

Symbol	Description	Values
V_{dc}	DC voltage. (V)	600
f_s	Switching frequency. (kHz)	10
L_f	LC filter inductance. (mH)	3
C_f	LC filter capacitance. (μF)	30
R_c	Line resistance. (Ω)	0
L_c	Line inductance. (mH)	DG #1(master): 4 DG #2(slave): 1 DG #3(slave): 3
ω_0	Nominal frequency. (rad/s)	100π
E_{b0}	Nominal PCC voltage. (V)	200
$[\omega_L, \omega_H]$	Frequency error band. (rad/s)	2π*[49.99, 50.01]
$[E_{bL}, E_{bH}]$	PCC voltage error band. (V)	[199, 201]
m_{pm}	Droop gain. (rad/s/W)	2e-4
n_{qm}	Droop gain. (V/var)	5e-3
m_{psi}	Droop gain. (W/(rad/s))	DG #2(slave):2500 DG #3(slave):2500
n_{qsi}	Droop gain. (var/V)	DG #2(slave): 100 DG #3(slave): 100
ω_{cm}, ω_{cs}	Cutoff frequency (rad/s)	8π
ω_f	Cutoff frequency (rad/s)	2π
α_p, α_q	Secondary control parameters.	0.3
β_p, β_q	Secondary control parameters.	2.5
γ_{psi}, γ_{qsi}	Power dispatch coefficients.	DG #2(slave): 0.50 DG #3(slave): 0.50
T_{d1}, T_{d2}, T_{d3}	Time intervals. (sec)	2

A. CASE 1: TRADITIONAL PI-BASED METHOD

Fig. 14 shows the results of traditional PI-based method. Both frequency and PCC voltage restores to their nominal values after the secondary control starting. However, power sharing error between the two slave DGs appears and accumulates at the same time. This error is result from the integral error in PI regulators and becomes much bigger when the load changes. As a result, the traditional PI-based method fails to guarantee power sharing among slave DGs while restoring frequency and PCC voltage.

B. CASE 2: PROPOSED METHOD AGAINST TRIGGERING DELAY

As Fig. 15(a) and (c) illustrate, after the system reaching steady state, the load demand increases by 3.8kW so that frequency decreases. When the frequency exceeds the error band, the secondary controllers of DG #2 and DG #3 are triggered with a 200 ms given triggering delay. However, the active power sharing error resulting from this triggering delay can be completely eliminated during PSM and frequency restores to the error band with accurate active power sharing between the two slave DGs. The results of PCC voltage restoration process are similar. In conclusion, the proposed method not only eliminates frequency and PCC voltage deviations but guarantees accurate power sharing among slave DGs. Meanwhile, the influence of any triggering delay among slave DGs can also be eliminated theoretically if the parameters are well designed.

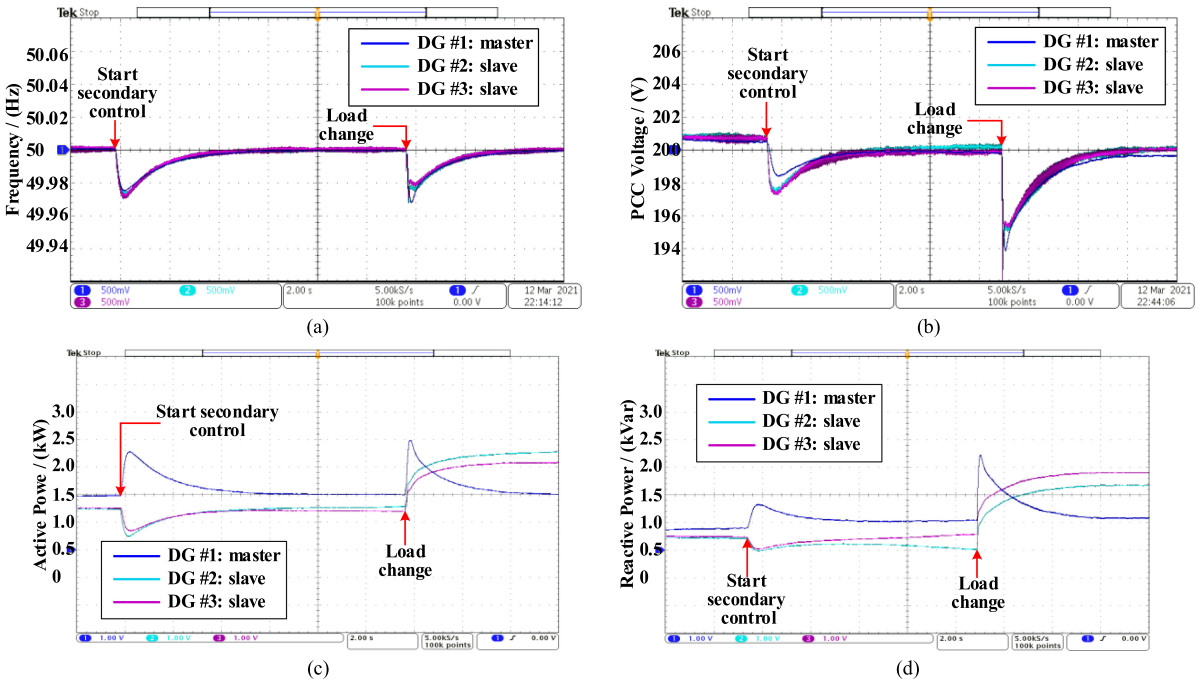

FIGURE 14. Experimental results of traditional PI based method: (a), (c) Frequency regulation, (b), (d) PCC voltage regulation.

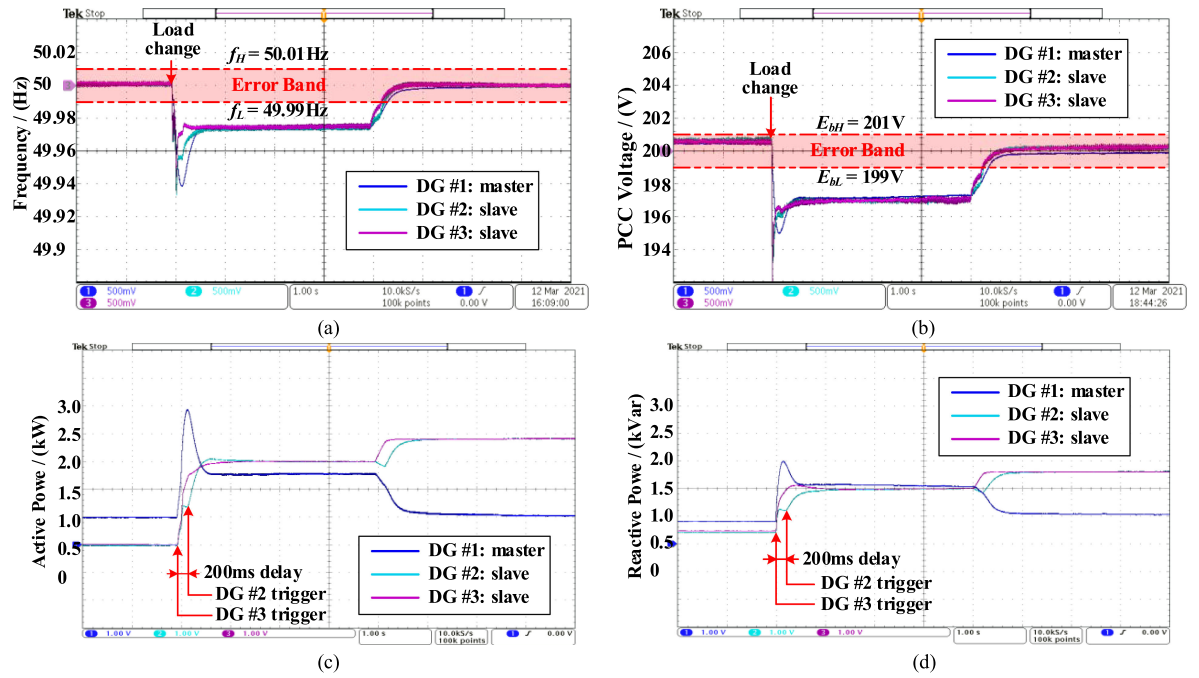

FIGURE 15. Experimental results of proposed method when DG #2 shows 200ms triggering delay: (a), (c) Frequency regulation, (b), (d) PCC voltage regulation.

C. CASE 3: RETRIGGERING OF THE PROPOSED METHOD

As Fig. 16(a) and (c) illustrate, the secondary controllers of DG #2 and #3 are triggered and switched from PSM, PEM to the RM after the load demand increases 2kW. However, the load demand changes again and decreases 2kW during RM. As a result, frequency increases and moves beyond the error band. Then, at the end of RM, the termination judgement process starts. The secondary controllers are retriggered and switched to PEM again since frequency is still out of the error band. Finally, frequency restores to the error band with accurate active power sharing among DG #2 and DG #3. The results are similar for PCC voltage restoration situation. In conclusion, the proposed method can still restore frequency and PCC voltage to the given error band and guarantee

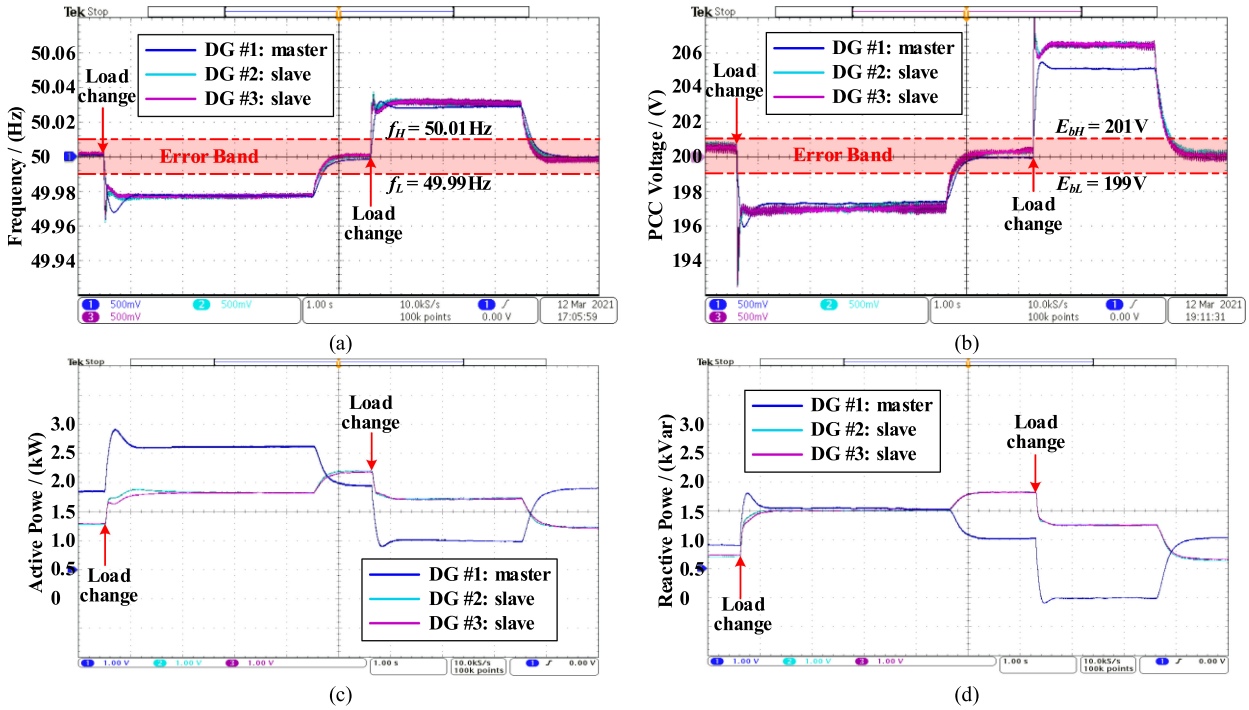

FIGURE 16. Experimental results of proposed method when load changes during secondary control: (a), (c) Frequency regulation, and (b), (d) PCC voltage regulation.

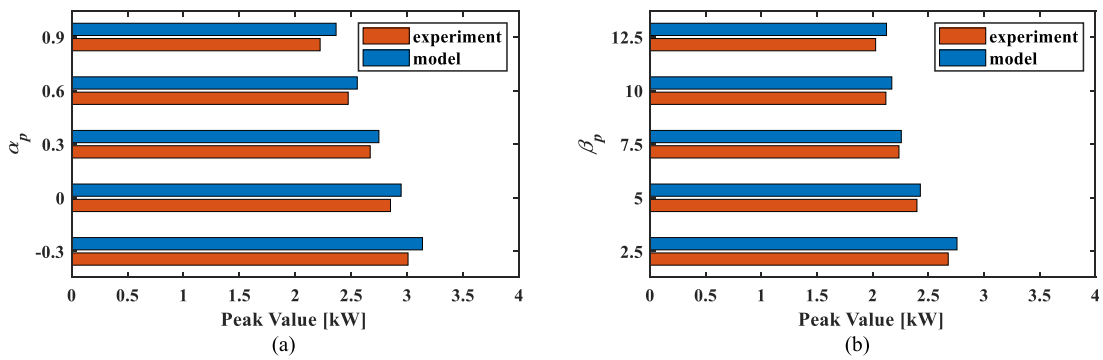

FIGURE 17. Peak value of master DG's output power when load demand shows step change in experimental test: (a) $\beta_p = 2.5$ and (b) $\alpha_p = 0.3$.

accurate power sharing among slave DGs at the same time, even if the load demand changes during the secondary control process.

D. CASE 4: MODEL VERIFICATION

Since the peak value of the master DG's output power during secondary control processes is a key parameter to determine the capacity of the master DG, this value is compared between the experimental results and the prediction of the model, as Fig. 17 shows. The peak value of master DG's output power predicted by the model is very close to but a little larger than the experimental result in each situation. This is because the model neglects dynamics of the circuit, the inner control loops and the SRF-PLLs, which contribute extra damping. Therefore, the damping of the model is small than the real system so that the peak value of the model is larger than the real system. As a result, the parameters designed based on the model is relatively conservative and works well in real system. Therefore, the model is accurate enough for parameters design purpose.

E. CASE 5: VOLTAGE AND CURRENT WAVEFORM

Figs. 18 and 19 shows the PCC voltage and output current waveforms of frequency restoration process during the transient processes and after the system reaching steady state respectively when the load increases 4kW. It is clear that both of the PCC voltage and output current waveforms show good dynamics without apparent overshoot. Meanwhile, the two

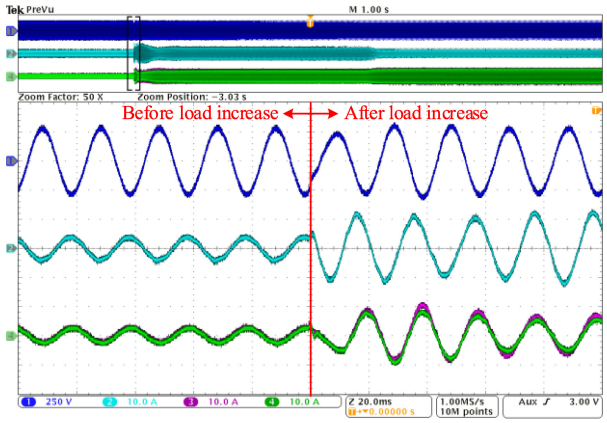

FIGURE 18. Experimental waveforms of frequency restoration process during transient process when load increases 4kW. CH1: line-to-line PCC voltage between phase-a and phase-c; CH2: phase-a output current of DG #1 (master); CH3: phase-a output current of DG #2 (slave); CH4: phase-a output current of DG #3 (slave).

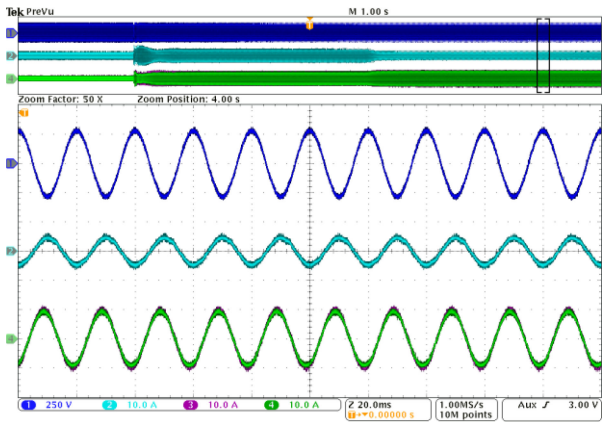

FIGURE 19. Experimental waveforms of frequency restoration process after system reaching steady state when load increases 4kW. CH1: line-to-line PCC voltage between phase-a and phase-c; CH2: phase-a output current of DG #1 (master); CH3: phase-a output current of DG #2 (slave); CH4: phase-a output current of DG #3 (slave).

salve DGs shares the same output current in steady state after the frequency restoration process.

VI. CONCLUSION

The HDMS structure takes the advantage of both droop control and master-slave control but causes frequency and voltage deviations in microgrids. To deal with this issue, this paper proposes a mode switching-based decentralized secondary control method implemented in slave DGs. The secondary controller switches among different modes to achieve different control goals in a time division manner. The proposed method can not only eliminate frequency and PCC voltage deviations but maintain accurate active and reactive power sharing among slave DGs in a communication-free manner. The influence of possible triggering delay among slave DGs can be completely eliminated. The effectiveness of the proposed method is verified by experiments.

REFERENCES

[1] A. Milczarek, M. Malinowski, and J. M. Guerrero, "Reactive power management in islanded microgrid—Proportional power sharing in hierarchical droop control," *IEEE Trans. Smart Grid*, vol. 6, no. 4, pp. 1631–1638, Jul. 2015.

[2] J. Rocabert, A. Luna, F. Blaabjerg, and P. Rodríguez, "Control of power converters in AC microgrids," *IEEE Trans. Power Electron.*, vol. 27, no. 11, pp. 4734–4749, Nov. 2012.

[3] J. M. Guerrero, L. Hang, and J. Uceda, "Control of distributed uninterruptible power supply systems," *IEEE Trans. Ind. Electron.*, vol. 55, no. 8, pp. 2845–2859, Aug. 2008.

[4] J.-F. Chen and C.-L. Chu, "Combination voltage-controlled and current-controlled PWM inverters for UPS parallel operation," *IEEE Trans. Power Electron.*, vol. 10, no. 5, pp. 547–558, Sep. 1995.

[5] A. Mortezaei, M. G. Simões, M. Savaghebi, J. M. Guerrero, and A. Al-Durra, "Cooperative control of multi-master–slave islanded microgrid with power quality enhancement based on conservative power theory," *IEEE Trans. Smart Grid*, vol. 9, no. 4, pp. 2964–2975, Jul. 2018.

[6] S. Wang, Z. Liu, J. Liu, R. An, and M. Xin, "Breaking the boundary: A droop and master-slave hybrid control strategy for parallel inverters in islanded microgrids," in *Proc. Energy Convers. Congr. Expo.*, 2017, pp. 3345–3352.

[7] S. Wang, Z. Liu, J. Liu, B. Liu, X. Meng, and R. An, "Modeling and analysis of droop based hybrid control strategy for parallel inverters in islanded microgrids," in *Proc. Appl. Power Electron. Conf. Expo.*, 2017, pp. 3462–3469.

[8] G. G. Talapur, H. M. Suryawanshi, A. B. Shitole, and P. Nachankar, "Combined droop and master-slave method for load sharing in standalone AC microgrid," in *Proc. 44th Annu. Conf. IEEE Ind. Electron. Soc.*, 2018, pp. 1705–1710.

[9] H. A. Sher, A. F. Murtaza, A. Noman, K. E. Addoweesh, K. Al-Haddad, and M. Chiaberge, "A new sensorless hybrid MPPT algorithm based on fractional short-circuit current measurement and P&O MPPT," *IEEE Trans. Sustain. Energy*, vol. 6, no. 4, pp. 1426–1434, Oct. 2015.

[10] Y. Khayat *et al.*, "On the secondary control architectures of AC microgrids: An overview," *IEEE Trans. Power Electron.*, vol. 35, no. 6, pp. 6482–6500, Jun. 2020.

[11] Y. Han, P. Shen, X. Zhao, and J. M. Guerrero, "An enhanced power sharing scheme for voltage unbalance and harmonics compensation in an islanded AC microgrid," *IEEE Trans. Energy Convers.*, vol. 31, no. 3, pp. 1037–1050, Sep. 2016.

[12] A. Bidram, A. Davoudi, F. L. Lewis, and J. M. Guerrero, "Distributed cooperative secondary control of microgrids using feedback linearization," *IEEE Trans. Power Syst.*, vol. 28, no. 3, pp. 3462–3470, Aug. 2013.

[13] F. Guo, C. Wen, J. Mao, and Y.-D. Song, "Distributed secondary voltage and frequency restoration control of droop-controlled inverter-based microgrids," *IEEE Trans. Ind. Electron.*, vol. 62, no. 7, pp. 4355–4364, Jul. 2015.

[14] N. M. Dehkordi, N. Sadati, and M. Hamzeh, "Fully distributed cooperative secondary frequency and voltage control of islanded microgrids," *IEEE Trans. Energy Convers.*, vol. 32, no. 2, pp. 675–685, Jun. 2017.

[15] M. Hua, H. Hu, Y. Xing, and J. M. Guerrero, "Multilayer control for inverters in parallel operation without intercommunications," *IEEE Trans. Power Electron.*, vol. 27, no. 8, pp. 3651–3663, Aug. 2012.

[16] M. Kim and A. Kwasinski, "Decentralized hierarchical control of active power distribution nodes," *IEEE Trans. Energy Convers.*, vol. 29, no. 4, pp. 934–943, Dec. 2014.

[17] M. Yazdanian and A. Mehrizi-Sani, "Washout filter-based power sharing," *IEEE Trans. Smart Grid*, vol. 7, no. 2, pp. 967–968, Mar. 2016.

[18] Y. Sun, X. Hou, J. Yang, H. Han, M. Su, and J. M. Guerrero, "New perspectives on droop control in AC microgrid," *IEEE Trans. Ind. Electron.*, vol. 64, no. 7, pp. 5741–5745, Jul. 2017.

[19] Y. Han, H. Li, L. Xu, X. Zhao, and J. M. Guerrero, "Analysis of washout filter-based power sharing strategy—An equivalent secondary controller for islanded microgrid without LBC lines," *IEEE Trans. Smart Grid*, vol. 9, no. 5, pp. 4061–4076, Sep. 2018.

[20] W. Gu, G. Lou, W. Tan, and X. Yuan, "A nonlinear state estimator-based decentralized secondary voltage control scheme for autonomous microgrids," *IEEE Trans. Power Syst.*, vol. 32, no. 6, pp. 4794–4804, Nov. 2017.

[21] Y. Wang, Z. Chen, X. Wang, Y. Tian, Y. Tan, and C. Yang, "An estimator-based distributed voltage-predictive control strategy for AC islanded microgrids," *IEEE Trans. Power Electron.*, vol. 30, no. 7, pp. 3934–3951, Jul. 2015.
[22] G. Lou, W. Gu, L. Wang, B. Xu, M. Wu, and W. Sheng, "Decentralised secondary voltage and frequency control scheme for islanded microgrid based on adaptive state estimator," *IET Gener. Transmiss.Distribution*, vol. 11, no. 15, pp. 3683–3693, 2017.
[23] B. Liu, T. Wu, Z. Liu, and J. Liu, "A small-AC-signal injection-based decentralized secondary frequency control for droop-controlled islanded microgrids," *IEEE Trans. Power Electron.*, vol. 35, no. 11, pp. 11634–11651, Nov. 2020.
[24] J. M. Rey, P. Martí, M. Velasco, J. Miret, and M. Castilla, "Secondary switched control with no communications for islanded microgrids," *IEEE Trans. Ind. Electron.*, vol. 64, no. 11, pp. 8534–8545, Nov. 2017.
[25] T. Wu, J. Liu, Z. Liu, S. Wang, and B. Liu, "Load power estimation based secondary control for microgrids," in *Proc. 9th Int. Conf. Power Electron. ECCE Asia*, 2015, pp. 722–727.
[26] *IEEE Standard for Interconnection and Interoperability of Distributed Energy Resources with Associated Electric Power Systems Interface*, IEEE Standard 1547-2018 Revis. IEEE Standard 1547-2003, pp. 1–138, Apr. 2018.

JIAZHI WANG (Graduate Student Member, IEEE) received the B.S. degree in electrical engineering and automation from Chongqing University, Chongqing, China, in 2019. He is currently working toward the Ph.D. degree with Xi'an Jiaotong University, Xi'an, China. His research interests include coordinative control and design of droop-based and virtual synchronous generator-based parallel inverters in ac microgrids.

ZENG LIU (Member, IEEE) received the B.S. degree in electrical engineering from Hunan University, Changsha, China, in 2006, and the M.S. and Ph.D. degrees in electrical engineering from Xi'an Jiaotong University (XJTU), Xi'an, China, in 2009 and 2013, respectively. He then joined XJTU as a Faculty Member in electrical engineering, where he is currently an Associate Professor. From 2015 to 2017, he was a Visiting Scholar with the Center for Power Electronics Systems, Virginia Polytechnic Institute and State University, Blacksburg, VA, USA. His research interests include control of power systems with multiple converters for renewable energy and energy storage applications, and small-signal stability of power electronics systems. He was the recipient of the two Prize Paper Awards in IEEE TRANSACTIONS ON POWER ELECTRONICS. He is an Associate Editor for the IEEE OPEN JOURNAL OF POWER ELECTRONICS and on the Editorial Board of the *Energies*, and was the Secretary-General of 2019 IEEE 10th International Symposium on Power Electronics for Distributed Generation Systems and *2020* The 4th International Conference on HVDC.

JINJUN LIU (Fellow, IEEE) received the B.S. and Ph.D. degrees in electrical engineering from Xi'an Jiaotong University (XJTU), Xi'an, China, in 1992 and 1997, respectively. He then joined the XJTU Electrical Engineering School as a Faculty. From late 1999 to early 2002, he was a Visiting Scholar with the Center for Power Electronics Systems, Virginia Polytechnic Institute and State University, Blacksburg, VA, USA. In late 2002, he was promoted as a Full Professor and then the Head of the Power Electronics and Renewable Energy Center, XJTU, which now comprises more than 20 faculty members and more than 200 graduate students and carries one of the leading power electronics programs, China. From 2005 to early 2010, he was an Associate Dean of the School of Electrical Engineering, XJTU, and from 2009 to early 2015, the Dean for Undergraduate Education of XJTU. He is currently a XJTU Distinguished Professor of power electronics. He has coauthored three books, including one textbook, authored or coauthored more than 500 technical papers in peer-reviewed journals and conference proceedings, holds 70 invention patents (China/U.S./EU), and delivered for many times plenary keynote speeches and tutorials at IEEE conferences or China national conferences. His research interests include modeling, control, and design methods for power converters and electronified power systems, power quality control and utility applications of power electronics, and micro-grids for sustainable energy and distributed generation. He was the recipient of many times governmental awards at national level or provincial/ministerial level for scientific research/teaching achievements. He was also the recipient of the 2006 Delta Scholar Award, 2014 Chang Jiang Scholar Award, 2014 Outstanding Sci-Tech Worker of the Nation Award, 2016 State Council Special Subsidy Award, IEEE Transactions on Power Electronics 2016 and 2021 Prize Paper Awards, and Nomination Award for the Grand Prize of 2020 Bao Steel Outstanding Teacher Award. He was the IEEE Power Electronics Society Region ten Liaison and then China Liaison for ten years, has been an Associate Editor for the IEEE TRANSACTIONS ON POWER ELECTRONICS since 2006, 2015–2019 Executive Vice President and 2020–2021 Vice President of IEEE PELS. He was on the Board of China Electrotechnical Society 2012–2020 and was elected the Vice President in 2013 and the Secretary General in 2018 of the CES Power Electronics Society. He was the Vice President of International Affairs, China Power Supply Society (CPSS) from 2013 to 2021, and since 2016, has been the inaugural Editor-in-Chief of *CPSS Transactions on Power Electronics and Applications*. He was elected the President of CPSS in November 2021. Since 2013, he has been the Vice Chair of the Chinese National Steering Committee for College Electric Power Engineering Programs.

TENG WU (Member, IEEE) received the B.S. and Ph.D. degrees in electrical engineering from Xi'an Jiaotong University, Xi'an, China, in 2012 and 2017, respectively. He is currently with the KINGSI Power Co., Ltd. His research focuses on the coordinative control of droop based paralleled converters in AC microgrids.